

Constraining the solar neighbourhood age-metallicity relation from white dwarf-main sequence binaries

A. Rebassa-Mansergas^{1,2*}, J. Maldonado³, R. Raddi¹, A. T. Knowles¹, S. Torres^{1,2}, M. Hoskin⁴, T. Cunningham⁴, M. Hollands⁴, J. Ren⁵, B. T. Gänsicke⁴, P.-E. Tremblay⁴, N. Castro-Rodríguez^{6,7,8}, M. Camisassa^{9,1}, D. Koester¹⁰

¹ *Departament de Física, Universitat Politècnica de Catalunya, c/Esteve Terrades 5, 08860 Castelldefels, Spain*

² *Institute for Space Studies of Catalonia, c/Gran Capità 2–4, Edif. Nexus 104, 08034 Barcelona, Spain*

³ *INAF - Osservatorio Astronomico di Palermo, Piazza del Parlamento 1, 90134 Palermo, Italy*

⁴ *Department of Physics, University of Warwick, Coventry, CV4 7AL, UK*

⁵ *CAS Key Laboratory of Space Astronomy and Technology, National Astronomical Observatories, Chinese Academy of Sciences, Beijing 100101, China*

⁶ *Instituto de Astrofísica de Canarias, E-38200, La Laguna, Tenerife, Spain*

⁷ *Universidad de La Laguna. Depart. de Astrofísica, E-38206, La Laguna, Tenerife, Spain*

⁸ *GRANTECAN, Cuesta de San José s/n, E-38712, Breña Baja, La Palma, Spain*

⁹ *Department of Applied Mathematics, University of Colorado, Boulder, CO 80309-0526, USA*

¹⁰ *Institut für Theoretische Physik und Astrophysik, Universität Kiel, 24098, Kiel, Germany*

Accepted XXX. Received YYY; in original form ZZZ

ABSTRACT

The age-metallicity relation is a fundamental tool for constraining the chemical evolution of the Galactic disc. In this work we analyse the observational properties of this relation using binary stars that have not interacted consisting of a white dwarf –from which we can derive the total age of the system– and a main sequence star –from which we can derive the metallicity as traced by the [Fe/H] abundances. Our sample consists of 46 widely separated, but unresolved spectroscopic binaries identified within the Sloan Digital Sky Survey, and 189 white dwarf plus main sequence common proper motion pairs identified within the second data release of *Gaia*. This is currently the largest white dwarf sample for which the metallicity of their progenitors have been determined. We find a flat age-metallicity relation displaying a scatter of [Fe/H] abundances of approximately ± 0.5 dex around the solar metallicity at all ages. This independently confirms the lack of correlation between age and metallicity in the solar neighbourhood that is found in previous studies focused on analysing single main sequence stars and open clusters.

Key words: stars: abundances – binaries: spectroscopic – stars: low-mass – white dwarfs – solar neighbourhood – techniques: spectroscopic

1 INTRODUCTION

The formation and assembly history of our Galaxy can be traced through the chemical composition, age, position and velocity of its constituent stars. In particular, the age-metallicity relation (AMR), that is the observed connection between the age and the chemical abundances of stars, can provide vital constraints on the formation and evolution of the Galactic disc. The AMR has therefore been widely-studied during the last decades (e.g. see the reviews of Nomoto et al. 2013 and Feltzing & Chiba 2013 and the more recent studies by Bergemann et al. 2014 and Wojno et al. 2018). Some of the very early works on this topic found evidence for an AMR in which the oldest stars have the lowest metallicity (e.g. Twarog 1980, Rocha-Pinto et al. 2000, Soubiran et al. 2008). This relation was found to behave as expected in a formation and evolution scenario in which stars form from the metal-enriched gas left by previous generations of stars. However, there have been evidence against an AMR exist-

ing at all, with large metallicity dispersions found in comprehensive or more recent works (e.g. Edvardsson et al. 1993; Haywood et al. 2013; Bergemann et al. 2014; Wu et al. 2021). The lack of correlation between age and metallicity in the Milky Way suggests a much more complicated formation scenario (Feuillet et al. 2019).

A major limitation of most previous studies is the measurement of stellar ages, which is a difficult task. Historically, the ages of stars were estimated through chromospheric activity levels (e.g. Barry 1988; Rocha-Pinto et al. 2000) or through isochrone fitting with an appropriate metallicity (e.g. Jørgensen & Lindegren 2005; Howes et al. 2019). More recently, the combination of spectroscopy and asteroseismology has been used to estimate stellar masses and to derive stellar ages (e.g. Casagrande et al. 2016; Pinsonneault et al. 2018).

An alternative method to estimate the age component of the AMR is to use white dwarfs (WDs) as cosmic clocks. WDs are the typical end stage of the vast majority of main sequence (MS) stars (see the review of Althaus et al. 2010), and because their evolution follows a relatively simple and well understood cooling process, they can be

* E-mail: alberto.rebassa@upc.edu

used as reliable observational measures of stellar age (e.g. [Fouesneau et al. 2019](#); [Qiu et al. 2020](#); [Lam et al. 2020](#)). In order to determine the total age of a WD, defined as the sum of its cooling age and its MS progenitor lifetime, two processes are required. First, a prescription for evolutionary cooling sequences provides a measure of the WD cooling age from observed determinations of effective temperature (T_{eff}) and surface gravity ($\log g$). To that end we adopt the widely-used sequences of the La Plata group (e.g. [Renedo et al. 2010](#); [Althaus et al. 2015](#); [Camisassa et al. 2016, 2019](#)), which encompass the full range of WD masses and the most updated prescriptions in the treatment of physical processes. Second, a relationship between the mass of the WD and the mass of its progenitor is required to obtain a MS lifetime estimate. This initial-to-final mass relation (e.g. [Catalán et al. 2008](#); [Cummings et al. 2018](#); [Barrientos & Chanamé 2021](#)) enables the estimation of MS star masses from measures of the current day WD masses, which in turn, can be used to determine the time spent on the MS from evolutionary sequences, provided the metallicity is known. Once we know the MS lifetimes and the cooling times, the total ages are determined as the sum of these two ages.

Because a significant fraction of known MS stars in our Galaxy are expected to be in multiple systems, particularly binaries (e.g. [Yuan et al. 2015](#)), and because the majority of MS stars end their lives as WDs, it follows that there exists a large number of binary systems consisting of a primary (more massive) star that has evolved to a WD, and a secondary MS star. The majority of these WDMS binary systems are expected to have orbital separations that are wide enough to avoid mass transfer episodes, thus allowing one to treat them as if they were isolated ([Willems & Kolb 2004](#)). These wide WDMS binary systems can therefore be considered as useful probes in the study of the Galactic AMR. An accurate age of the WD can be estimated via the process described above and the MS star metallicity can be measured via detailed spectroscopic matching to stellar models (e.g. [Bensby et al. 2014](#); [Holtzman et al. 2015](#)). Assuming the two stars within the binary are coeval, a measurement of the WD age also gives an age estimate for the MS star, and thus the AMR can be probed using these systems. This work follows on from the initial study of [Rebassa-Mansergas et al. \(2016b\)](#), in which an AMR was determined from a pilot sample of 23 wide WDMS binary systems identified within the Sloan Digital Sky Survey (SDSS; [York et al. 2000](#); [Eisenstein et al. 2011](#)). Here, we continue this observational campaign and considerably enlarge the sample using WDMS binaries in resolved common proper motion pairs (CPMPs) identified thanks to the *Gaia* mission ([Gaia Collaboration et al. 2016](#)).

The structure for this paper is as follows. Section 2 presents the WDMS binary samples used for this work. Section 3 describes the observations of both WDs and MS stars. Section 4 presents the results, which are discussed in Section 5. Finally, Section 6 presents our conclusions.

2 THE WDMS BINARY SAMPLES

In this work we use two different WDMS binary samples to constrain the age-metallicity relation.

The first is the catalogue of more than 3000 WDMS binaries from the SDSS ([Rebassa-Mansergas et al. 2016a](#)). In particular, for this project we select binaries containing a hydrogen-rich white dwarf primary that display no significant radial velocity variations over a baseline of at least two days and have SDSS g magnitudes < 19 mag. The first requirement ensures the binaries are widely separated and therefore very likely did not evolve through any phase of mass transfer (note that the orbital period distribution of close SDSS WDMS

binaries peaks at ≈ 8 hours and that there are very few close binaries with periods longer than 1 day, see [Nebot Gómez-Morán et al. 2011](#)). The second condition selects systems that are bright enough to allow for the derivation of reliable WD ages and MS star metallicities from spectroscopic observations at ground-based telescopes of medium and large apertures. In [Rebassa-Mansergas et al. \(2016b\)](#) we presented a pilot study of the age-metallicity relation from 23 SDSS WDMS binaries and here we extend the analysis to 29 additional systems.

We build our second WDMS binary sample by mining the data release 2 of *Gaia* ([Gaia Collaboration et al. 2016, 2018a](#)). Our approach here is to identify CPMPs that contain a WD and a MS star. This has two clear advantages over the SDSS WDMS binary sample introduced in the previous paragraph. Firstly, the WD and MS stars are separated enough to allow for independent observations of the two stellar components. This avoids any possible selection effects against the identification of binaries containing cool WDs, which are generally outshined by the MS companions in the SDSS sample ([Rebassa-Mansergas et al. 2016a](#)). These WDs are of great interest since they have the longest cooling ages and can hence be used to test the age-metallicity relation at the intermediate/old ages. Secondly, the MS companions are not only M dwarfs, which are the dominant spectral types in the SDSS WDMS binary sample, but also F, G and K-type stars. M-dwarf metallicity calibrators that are based on the spectral analysis have been often criticised. For example, [Lindgren & Heiter \(2017\)](#) argue that, for individual M stars, different metallicity calibrations yield $[\text{Fe}/\text{H}]$ abundances that differ by as much as 0.6 dex. The *Gaia* WDMS binary sample containing F, G and K companions allows us to avoid this possible issue, since it has been shown that metallicity calibrations provide similar values of $[\text{Fe}/\text{H}]$ for such stars (e.g. [Teixeira et al. 2016](#)).

We searched for CPMP companions to the WDs that were identified by [Gentile Fusillo et al. \(2019\)](#) in *Gaia* DR2. From their catalogue, we selected 103,002 candidates with a probability of being a WD larger than 50 percent and a parallax uncertainty of better than 10 percent. Thus, we mined the *Gaia* DR2 archive searching for common proper motion MS companions within 100,000 au from the WD candidates. Our procedure mimics that of [El-Badry & Rix \(2018\)](#), although we used an input WD list and we adopted a wider search radius. By assuming the two stars are on a bound Keplerian orbit (cf. [Andrews et al. 2017](#); [El-Badry & Rix 2018](#); [Jiménez-Esteban et al. 2019](#)), we impose an upper limit of $8.5 M_{\odot}$ for the total mass of the system, which implies a maximum difference in projected velocities of ΔV_{\perp} (km/s) $\leq 2.73 \times (a/10^3 \text{ au})^{-1/2}$, where a is the projected separation in astronomical units. We applied standard astrometric and photometric cuts ([Gaia Collaboration et al. 2018b](#); [Lindgren 2018](#)) to ensure that companions with good quality data are found. Hence, we identify 4,415 WDMS systems with distances $\lesssim 500$ pc, with a log-normal distribution centered at $\log(1/\varpi) = 2.17 \pm 0.25$, where 0.25 is the standard deviation and ϖ is the measured parallax. A comparison with the catalogue of [El-Badry & Rix \(2018\)](#) shows that our search resulted in ≈ 1800 additional systems, while our catalogue does not contain 194 systems found by these authors. These differences are mostly explained by the use of an input WD list, which enables us to expand our catalogue towards larger distances from the Sun. A comparison with the most recent catalogue of common proper motion pairs identified by [El-Badry et al. \(2021\)](#) confirms a 92 percent overlap, with the majority of pairs having a

¹ $[\text{Fe}/\text{H}] = \log \left(\frac{n_{\text{Fe}}}{n_{\text{H}}} \right)_{*} - \log \left(\frac{n_{\text{Fe}}}{n_{\text{H}}} \right)_{\odot}$, where $\left(\frac{n_{\text{Fe}}}{n_{\text{H}}} \right)$ is the number abundance ratio of Fe relative to H for a given star (*) or for the Sun (\odot).

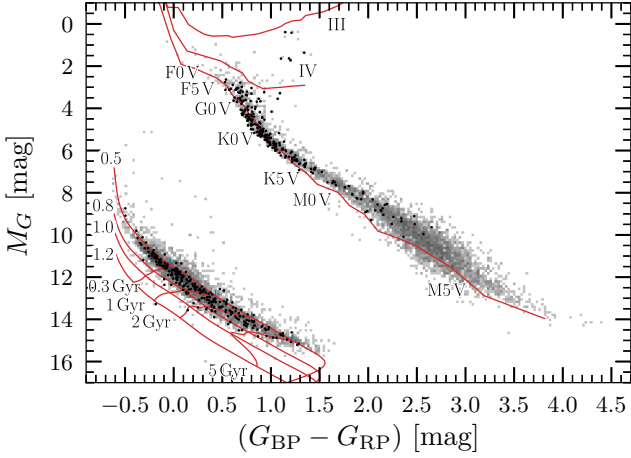


Figure 1. Hertzsprung-Russell diagram of *Gaia*-selected WDMS common proper-motion pairs. The dwarf (V), sub-giant (IV), and giant (III) tracks are obtained from the Pickles (1998) spectral library. The cooling sequences for hydrogen-rich WDs of 0.5, 0.8, 1.0, and 1.2 M_{\odot} are described by Camisassa et al. (2016) and Camisassa et al. (2019). The isochrones for total WD ages, that is the pre-WD evolutionary time and the WD cooling age, are also shown for 0.3, 1, 2, and 5 Gyr. The black dots represent the companion stars with available [Fe/H] abundances from our spectroscopic follow-up and their WD primaries.

low probability of chance alignment as defined by the authors. The Hertzsprung-Russell diagram of our resolved CPMP candidates is shown in Fig. 1.

3 OBSERVATIONS OF THE WDMS BINARY SAMPLE

We adopted different strategies to observe the WDMS binaries belonging to the two samples described in the previous section. A log of the observations is shown in Table 1.

SDSS WDMS binaries are unresolved despite the fact that they display no radial velocity variations. This is because they are generally located at far enough distances (≈ 400 – 500 pc; Rebassa-Mansergas et al. 2010). Therefore, one single spectrum collects the dispersed light from both components.

The *Gaia* WDMS binaries we selected in this work are members of spatially resolved CPMPs. As a consequence, we aimed at obtaining one optical spectrum for each component.

3.1 SDSS WDMS binaries

3.1.1 Very Large Telescope

We observed 17 SDSS WDMS binaries with the Very Large Telescope (VLT), at Cerro Paranal (Chile) and the X-Shooter instrument (Vernet et al. 2011). X-Shooter provides spectra in three arms simultaneously covering a wavelength range of $\approx 3,000$ – $25,000$ Å (UVB arm; 3,000–5,600 Å, VIS arm; 5,500–10,200 Å, NIR arm; 10,200–24,800 Å). The observations were performed in service mode using the 0.9–1" slits, which resulted in spectra with resolving power 4,350/7,450/5,300 in the UVB/VIS/NIR arms, respectively. We reduced and calibrated the data using the ESOREFLEX X-Shooter pipeline, version 3.3.5.

Table 1. Log of the observations including the telescope name, the observing mode (service, sm, or visitor, vm) the month dates or period of the observations, the instrument used and the number of taken spectra.

Telescope	Mode	Dates or period	Instrument #spec
VLT	sm	P101	X-Shooter 17
GTC	sm	2016B, 2017A	OSIRIS 10
GTC	sm	2017B, 2018A	EMIR 12
WHT	vm	Oct. 2018, Feb. & Apr. 2019	ISIS 122
INT	vm	Jul. 2019	IDS 92
TNG	sm	2018B	HARPS-N 106
Mercator	vm	Dec. 2018 & Jan. 2019	HERMES 377
Xinglong2.16	vm	Dec. 2018, Feb. 2019 & June 2020	echelle 51

3.1.2 Gran Telescopio Canarias

We obtained service mode optical and near-infrared spectra with the Gran Telescopio Canarias (GTC), for 10 and 12 additional SDSS WDMS binaries using the OSIRIS and EMIR instruments, respectively. We used the 2,000B and 2,500R gratings together with the 0.6 arcsec slit width for the optical OSIRIS observations, which resulted in optical spectra covering the 3,960–5,690 Å and 5,590–7,680 Å wavelength ranges at resolving powers of 2,000 and 2,500. The EMIR observations were performed using the K grism and the 0.8 arcsec slit width, thus providing spectra covering the 20,300–23,850 Å wavelength range at a resolving power of 3,100. The OSIRIS spectra were reduced using the PAMELA software (Marsh 1989) and calibrated using MOLLY². The EMIR spectra were reduced and calibrated using REDEMIR, a new GTC pipeline written in python. In a first step it eliminates the contribution of the sky background using consecutive A-B pairs. Subsequently, the spectra are flat-fielded, calibrated in wavelength and combined to obtain the final spectrum in the K band.

3.2 *Gaia* WDMS CPMPs

3.2.1 William Herschel Telescope

Low-resolution spectra for 122 WDs were obtained at the 4.2-meter William Herschel Telescope (WHT) at El Roque de los Muchachos observatory in La Palma in visitor mode during 2018 and 2019. We used the ISIS (Intermediate-dispersion Spectrograph and Imaging System) instrument and the 1 arcsec width long-slit together with two different gratings, the 600B and 600R. This provided blue- and red-arm simultaneous spectra at a resolving power of 600, respectively covering the $\approx 3,600$ – $5,100$ Å and $\approx 5,600$ – $7,200$ Å wavelength ranges. Arc spectra were taken along the nights to account the flexure of the instrument. The WHT spectra were reduced and calibrated using the PAMELA and MOLLY softwares, respectively.

3.2.2 Isaac Newton Telescope

Low-resolution spectra of 92 additional WDs were obtained at the Isaac Newton Telescope (INT) at El Roque de los Muchachos observatory in visitor mode in July 2019. We used the Intermediate Dispersion Spectrograph (IDS) and the R632V grating together with a 1 arcsec slit width. The spectra covered the $\approx 3,500$ – $6,000$ Å wavelength

² The MOLLY package is developed by Tom Marsh and is available at <http://deneb.astro.warwick.ac.uk/phsaap/software>.

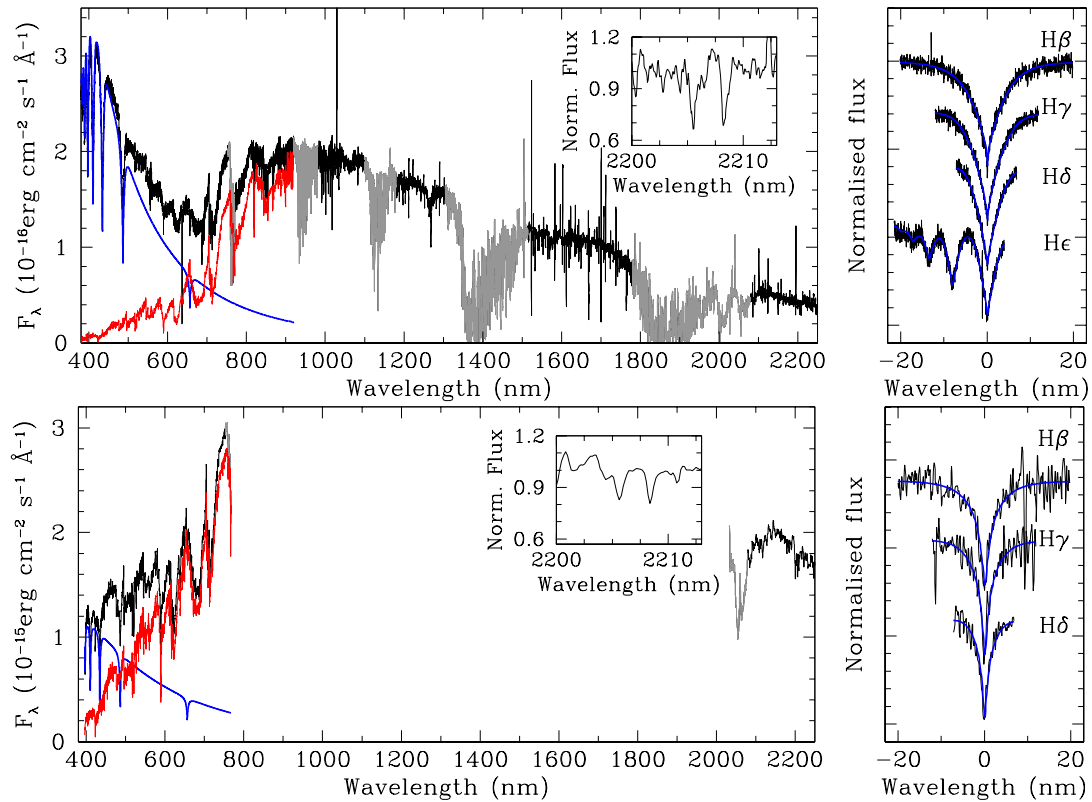


Figure 2. Top-left panel: spectrum of SDSSJ 0335+0038 (black) taken with X-Shooter. The telluric absorption regions are shown in grey. At blue wavelengths ($\lambda < 600$ nm) the flux contribution is dominated by the WD. Conversely, the red and near-infrared regions are dominated by the flux of the MS companion. In blue and red solid lines we show the best-fitting WD model and MS star template, respectively. The top right corner shows the 2205/2209 nm Na I absorption doublet (free of telluric absorption) used to estimate the $[\text{Fe}/\text{H}]$ abundance of the MS star. Top-right panel: the normalized residual and normalised WD Balmer lines ($\text{H}\beta$, $\text{H}\gamma$, $\text{H}\delta$, $\text{H}\epsilon$) resulting from subtracting the MS star together with the WD model (blue) that best fits the spectrum. Bottom panels: the same but for SDSSJ 1510+4048, which was observed with OSIRIS and EMIR mounted at the GTC. Note that the EMIR spectrum in the near-infrared is not flux calibrated and has been normalised to the average optical flux.

range at a resolving power of 2,500 and were reduced/calibrated using the PAMELA/MOLLY softwares.

3.2.3 Telescopio Nazionale Galileo

Service mode observations were carried out at the Telescopio Nazionale Galileo at El Roque de los Muchachos observatory to acquire 106 MS high-resolution spectra. We used the HARPS-N (High Accuracy Radial velocity Planet Searcher – North; Cosentino et al. 2012) spectrograph together with the 1 arcsec fibre, resulting in the wavelength coverage of $\approx 3,800\text{--}6,900$ Å. The resolving power of HARPS-N is 115,000. In order to wavelength calibrate the data we used arc-lamp spectra taken with a second fibre. The data were reduced and calibrated using the automated HARPS-N pipeline.

3.2.4 Mercator Telescope

We obtained 377 high-resolution MS spectra with the 1.2 m Mercator telescope located at the El Roque de los Muchachos observatory. We used the HERMES spectrograph (Raskin et al. 2011), which provided spectra covering the $3,770\text{--}9,000$ Å range in a single exposure at a resolving power of 85,000. The observations were performed under the high-resolution (HRS) mode and the data were reduced using

the dedicated automated data reduction pipeline and radial velocity toolkit (HermesDRS)³.

3.2.5 Xinglong 2.16m Telescope

Observations at the 2.16 meter telescope located at the Xinglong National Station (China) were performed in visitor mode during 2018 and 2019 to acquire 51 high-resolution MS spectra. We used the High Resolution fiber-fed Spectrograph (HRS) (Fan et al. 2016), which provided echelle spectra covering the $\approx 3,650\text{--}10,000$ Å wavelength range at a resolving power of 49,800. Thorium-argon arc spectra were taken at the beginning and the end of each night. The data were reduced and calibrated using the IRAF package (Tody 1986).

4 METHODOLOGY AND RESULTS

In this section we provide details on how we derive the WD ages and MS star metallicities, i.e. $[\text{Fe}/\text{H}]$ abundances. The results are presented in Table 2 for the SDSS WDMS binary sample and in Table 3 for the *Gaia* WDMS CPMPs.

³ Publicly available at <http://www.mercator.iac.es/instruments/hermes/drs/>

Table 2. List of objects, right ascension and declination of the 52 SDSS WDMS binaries containing hydrogen-rich WDs studied in this work. For 46 of them we can derive the WD total ages. We also indicate the WD effective temperatures, surface gravities and masses as well as the M dwarf spectral types (Sp) that have been obtained from our spectral fitting routine. The instruments used in the observations are indicated too. WD total ages and MS star [Fe/H] abundances are given in columns 8 and 9, respectively. The WD parameters of SDSSJ 0648+3810 and SDSSJ 2228+3912 are derived fitting the available SDSS spectra. The age and WD parameters age of SDSSJ 0138-0016 are obtained from [Parsons et al. \(2012\)](#).

Object	ra (degrees)	dec (degrees)	T_{eff} (WD) (K)	$\log g$ (WD) (dex)	Mass (WD) (M_{\odot})	Sp (MS)	Age (Gyr)	[Fe/H] (dex)	Instr.
SDSSJ 0021-1103	5.49125	-11.05878	10718±9	8.59±0.03	0.96 ^{+0.02} _{-0.01}	M4	1.35 ^{+0.09} _{-0.08}	0.26±0.12	X-Shooter
SDSSJ 0054+0057	13.57725	0.96281	19729±42	7.83±0.01	0.543 ^{+0.004} _{-0.004}	M4	4.731 ^{+0.010} _{-0.003}	0.22±0.12	X-Shooter
SDSSJ 0328+0017	52.17883	0.29714	12885±532	7.86±0.13	0.54 ^{+0.06} _{-0.05}	M2	8.51 ^{+3.48} _{-2.61}	0.56±0.12	X-Shooter
SDSSJ 0335+0038	53.95242	0.64228	17993±19	7.92±0.01	0.581 ^{+0.004} _{-0.004}	M4	3.62 ^{+0.39} _{-0.39}	0.05±0.12	X-Shooter
SDSSJ 1005+2112	151.26421	21.20111	20658±26	7.91±0.01	0.572 ^{+0.005} _{-0.005}	M2	4.14 ^{+0.1} _{-0.25}	0.25±0.12	X-Shooter
SDSSJ 1114+0838	168.58033	8.64140	11752±59	8.16±0.03	0.70 ^{+0.02} _{-0.02}	M5	0.98 ^{+0.04} _{-0.04}	-0.38±0.12	X-Shooter
SDSSJ 1117+0129	169.39633	1.49439	9018±10	8.25±0.03	0.74 ^{+0.02} _{-0.02}	M6	1.60 ^{+0.04} _{-0.02}	0.15±0.12	X-Shooter
SDSSJ 1120+1901	170.05296	19.02412	13035±1263	7.86±0.24	0.53 ^{+0.13} _{-0.10}	M3	8.00 ^{+4.00} _{-5.60}	0.17±0.12	X-Shooter
SDSSJ 1417+1301	214.41758	13.03014	34682±20	7.39±0.01	0.44 ^{+0.01} _{-0.01}	M4	-	0.17±0.12	X-Shooter
SDSSJ 1453+0010	223.27405	0.18008	12025±83	8.32±0.03	0.80 ^{+0.02} _{-0.02}	M4	0.86 ^{+0.06} _{-0.04}	0.16±0.12	X-Shooter
SDSSJ 1557+1442	239.33622	14.70491	12165±12	7.87±0.03	0.54 ^{+0.01} _{-0.01}	M5	8.67 ^{+2.14} _{-1.19}	-0.17±0.12	X-Shooter
SDSSJ 1601+0505	240.40292	5.09108	44479±343	7.87±0.03	0.61 ^{+0.01} _{-0.01}	M1	1.82 ^{+0.38} _{-0.39}	0.22±0.12	X-Shooter
SDSSJ 1731+0703	262.76886	7.06251	11888±27	8.60±0.03	0.97 ^{+0.02} _{-0.02}	M4	1.04 ^{+0.06} _{-0.04}	-0.61±0.12	X-Shooter
SDSSJ 2044-0614	311.13100	-6.24450	16792±162	7.76±0.03	0.51 ^{+0.01} _{-0.01}	M1	-	-0.36±0.12	X-Shooter
SDSSJ 2312+0053	348.12829	0.88933	29181±39	8.12±0.02	0.70 ^{+0.01} _{-0.01}	M2	0.43 ^{+0.03} _{-0.03}	-0.06±0.12	X-Shooter
SDSSJ 2342+1559	355.60696	15.99175	12885±45	8.06±0.03	0.64 ^{+0.02} _{-0.02}	M5	0.99 ^{+0.05} _{-0.05}	-0.61±0.12	X-Shooter
SDSSJ 2350+0043	357.61496	0.73297	12885±2013	7.89±0.35	0.55 ^{+0.20} _{-0.15}	M2	6.61 ^{+5.39} _{-0.83}	-0.40±0.12	X-Shooter
SDSSJ 0648+3810	102.05319	38.16831	20098±1341	7.97±0.24	0.61 ^{+0.13} _{-0.10}	M1	1.30 ^{+0.90} _{-1.29}	-0.55±0.12	SDSS/EMIR
SDSSJ 1241+6007	190.41985	60.11985	23076±426	7.75±0.07	0.52 ^{+0.02} _{-0.02}	M3	-	-0.39±0.12	Osiris/EMIR
SDSSJ 1510+4048	227.69042	40.80750	9573±40	8.45±0.07	0.87 ^{+0.04} _{-0.05}	M2	1.50 ^{+0.16} _{-0.10}	-0.50±0.12	Osiris/EMIR
SDSSJ 1521+2450	230.31696	24.83787	36154±149	7.91±0.04	0.61 ^{+0.02} _{-0.02}	M2	1.71 ^{+0.55} _{-1.22}	0.19±0.12	Osiris/EMIR
SDSSJ 1525+3629	231.32454	36.49589	9681±35	7.61±0.07	0.42 ^{+0.03} _{-0.03}	M4	-	-0.3±0.12	Osiris/EMIR
SDSSJ 1600+3626	240.24929	36.43608	23076±172	7.85±0.03	0.56 ^{+0.01} _{-0.01}	M5	5.05 ^{+1.66} _{-2.03}	-0.12±0.12	Osiris/EMIR
SDSSJ 1605+4610	241.41737	46.17939	33740±280	7.97±0.05	0.64 ^{+0.03} _{-0.02}	M0	0.63 ^{+0.10} _{-0.12}	-0.78±0.12	Osiris/EMIR
SDSSJ 1624+3217	246.20417	32.28389	89774±688	8.15±0.07	0.76 ^{+0.04} _{-0.04}	M1	0.06 ^{+0.06} _{-0.05}	-0.30±0.12	Osiris/EMIR
SDSSJ 1624+3648	246.03358	36.81625	25012±205	7.99±0.03	0.63 ^{+0.01} _{-0.01}	M3	0.73 ^{+0.10} _{-0.25}	-0.36±0.12	Osiris/EMIR
SDSSJ 1833+6431	278.37162	64.53104	54094±867	7.90±0.05	0.65 ^{+0.02} _{-0.02}	M2	0.59 ^{+0.08} _{-0.09}	-0.51±0.12	Osiris/EMIR
SDSSJ 1834+4137	278.72116	41.63269	9456±24	8.12±0.05	0.67 ^{+0.03} _{-0.03}	M4	1.42 ^{+0.03} _{-0.03}	-0.85±0.12	Osiris/EMIR
SDSSJ 2228+3912	337.09474	39.21106	25794±1745	7.81±0.24	0.55 ^{+0.12} _{-0.08}	M3	7.23 ^{+4.71} _{-1.46}	0.06±0.12	SDSS/EMIR
SDSSJ 0003-0503*	0.98723	-5.05909	19967±131	8.07±0.02	0.66 ^{+0.01} _{-0.01}	M4	0.72 ^{+0.11} _{-0.11}	0.05±0.12	X-Shooter
SDSSJ 0005-0544*	1.49948	-5.73780	32748±224	7.73±0.03	0.53 ^{+0.01} _{-0.01}	M2	8.27 ^{+0.07} _{-0.28}	0.06±0.12	X-Shooter
SDSSJ 0036+0700*	9.01079	7.01311	36105±49	7.87±0.02	0.589 ^{+0.009} _{-0.009}	M4	3.89 ^{+0.94} _{-0.95}	0.30±0.12	X-Shooter
SDSSJ 0052-0051*	13.03508	-0.85961	11933±94	8.02±0.03	0.61 ^{+0.02} _{-0.02}	M4	1.53 ^{+0.23} _{-0.52}	0.06±0.12	X-Shooter
SDSSJ 0111+0009*	17.84954	0.15981	12326±47	7.76±0.03	0.50 ^{+0.01} _{-0.01}	M2	-	-0.46±0.12	X-Shooter
SDSSJ 0138-0016*	24.71475	-0.27267	3570±110	7.92±0.02	0.54 ^{+0.01} _{-0.01}	M5	9.50 ^{+0.30} _{-0.20}	-0.56±0.12	X-Shooter
SDSSJ 0256-0730*	44.04421	-7.50683	10194±68	8.84±0.04	1.09 ^{+0.02} _{-0.02}	M5	1.99 ^{+0.02} _{-0.02}	-0.27±0.12	X-Shooter
SDSSJ 0258+0109*	44.57446	1.16278	36873±123	7.75±0.02	0.540 ^{+0.007} _{-0.007}	M3	5.87 ^{+0.05} _{-0.39}	0.23±0.12	X-Shooter
SDSSJ 0321-0016*	50.40225	-0.27511	31096±32	7.88±0.02	0.584 ^{+0.009} _{-0.008}	M5	2.95 ^{+0.88} _{-0.88}	0.17±0.12	X-Shooter
SDSSJ 0325-0111*	51.29517	-1.18725	10499±14	8.13±0.04	0.68 ^{+0.02} _{-0.02}	M2	1.19 ^{+0.03} _{-0.04}	-0.36±0.12	X-Shooter
SDSSJ 0331-0054*	52.88383	-0.91483	30742±30	7.96±0.01	0.622 ^{+0.005} _{-0.005}	M3	1.07 ^{+0.08} _{-0.08}	0.09±0.12	X-Shooter
SDSSJ 0824+1723*	126.12092	17.39594	12476±52	7.86±0.03	0.54 ^{+0.01} _{-0.01}	M3	9.40 ^{+2.33} _{-0.33}	-0.10±0.12	X-Shooter
SDSSJ 0832-0430*	128.23002	-4.51285	16064±85	8.01±0.01	0.623 ^{+0.006} _{-0.005}	M1	0.85 ^{+0.02} _{-0.47}	-0.76±0.12	X-Shooter
SDSSJ 0916-0031*	139.00617	-0.52494	19130±63	8.30±0.02	0.79 ^{+0.01} _{-0.01}	M4	0.46 ^{+0.05} _{-0.01}	0.30±0.12	X-Shooter
SDSSJ 0933+0926*	143.29962	9.44508	30401±18	7.63±0.01	0.50 ^{+0.002} _{-0.002}	M5	-	-0.07±0.12	X-Shooter
SDSSJ 1023+0427*	155.89271	4.45617	20498±68	7.89±0.02	0.56 ^{+0.01} _{-0.01}	M4	4.21 ^{+0.42} _{-0.21}	0.18±0.12	X-Shooter
SDSSJ 1040+0834*	160.23950	8.57267	10254±8	8.00±0.03	0.60 ^{+0.02} _{-0.02}	M5	1.55 ^{+0.23} _{-0.31}	-0.09±0.12	X-Shooter
SDSSJ 1405+0409*	211.39554	4.15183	20716±88	8.15±0.02	0.71 ^{+0.02} _{-0.01}	M4	0.51 ^{+0.03} _{-0.03}	-0.30±0.12	X-Shooter
SDSSJ 1527+1007*	231.93379	10.12289	34079±52	7.86±0.02	0.588 ^{+0.009} _{-0.009}	M3	1.31 ^{+0.24} _{-1.30}	-0.17±0.12	X-Shooter
SDSSJ 1539+0922*	234.89431	9.37265	11183±143	8.72±0.03	1.04 ^{+0.02} _{-0.02}	M5	1.53 ^{+0.02} _{-0.29}	0.29±0.12	X-Shooter
SDSSJ 1558+0231*	239.72171	2.52731	30062±9	7.79±0.01	0.548 ^{+0.004} _{-0.003}	M4	7.24 ^{+0.38} _{-0.29}	0.07±0.12	X-Shooter
SDSSJ 1624-0022*	246.13192	-0.38006	26291±203	7.92±0.03	0.60 ^{+0.01} _{-0.01}	M3	1.40 ^{+0.30} _{-0.45}	0.02±0.12	X-Shooter
SDSSJ 2341-0947*	355.49262	-9.78794	9433±26	8.27±0.04	0.76 ^{+0.02} _{-0.02}	M4	1.41 ^{+0.02} _{-0.02}	0.07±0.12	X-Shooter

Those systems that are reanalysed from [Rebassa-Mansergas et al. \(2016b\)](#) are indicated by * after their names.

4.1 M dwarf metallicities of the SDSS WDMS binary sample

We obtained the M dwarf [Fe/H] abundances from their *K*-band, near-infrared X-Shooter and EMIR spectra following the procedure described in [Newton et al. \(2014\)](#). Note that at these wavelengths the WD contributions are negligible (see [Figure 2](#)). This method uses a semi-empirical multivariate linear regression based on the equivalent width of the 2,205/2,209 nm Na I absorption doublet to yield [Fe/H] values with an accuracy of 0.12 dex. To derive the equivalent width values we corrected the systemic (radial) velocities and we normalized the fluxes in the 2,194–2,220 nm wavelength range fitting a third-order spline function. In this process we excluded the Na I doublet absorption feature. We then used the trapezoidal rule to integrate the flux within the 2,204–2,210 nm region of the absorption doublet.

4.2 WD ages of the SDSS WDMS binary sample

We first run a decomposition/fitting routine to the optical X-Shooter and OSIRIS spectra of the binaries to determine the spectral type of the M dwarfs and subtract their flux contribution (left panels of [Figure 2](#), for details see [Rebassa-Mansergas et al. 2007](#)). The normalised Balmer lines of the residual WD spectra were then fitted with a grid of hydrogen-rich WD model atmosphere spectra ([Koester 2010](#), and unpublished improvements) in order to measure T_{eff} and $\log g$ (see the right panels of [Figure 2](#)). When appropriate, we accounted for the 3D corrections provided by [Tremblay et al. \(2013\)](#) and, thus, we linearly interpolated these values in the cooling sequences developed by the La Plata Group for three different metallicities ($Z=0.001$, [Althaus et al. 2015](#); $Z=0.01$, [Renedo et al. 2010](#); and $Z=0.02$, [Camisassa et al. 2016](#)) to obtain the WD masses and total ages, i.e. WD cooling plus MS progenitor lifetime⁴. The WD evolutionary sequences for $Z=0.001$ and $Z=0.02$ were derived from the full evolutionary history of their progenitor stars, from the Zero-Age-MS all the way to the WD phase. These WD models take into account all the relevant energy sources that govern the WD evolution, including the energy released by the crystallization process, as latent heat and as gravitational energy by the phase separation process. The progenitor lifetimes adopted in these sequences were interpolated from [Table 2](#) of [Miller Bertolami \(2016\)](#) and they adopted the initial-to-final mass relation of the same work, which is similar to the semi-empirical relations found in [Catalán et al. \(2008\)](#); [Cummings et al. \(2018\)](#). The sequences of [Renedo et al. \(2010\)](#) for $Z=0.01$ take into account all the relevant processes involved in the WD evolution, however they do not provide the progenitor lifetimes. We obtained those interpolating from [Table 2](#) of [Miller Bertolami \(2016\)](#).

Given that we know the [Fe/H] abundances ([Section 4.1](#)), and hence the Z values⁵, of the MS companions (assumed to be the same for the WD progenitors), we interpolated the measured Z between the three Z /total-age pairs obtained for each system from the evolutionary WD sequences to derive the corresponding total ages. In the cases where the metallicities were larger than 0.02 (the highest value provided by the models), we linearly extrapolated the ages from the

⁴ The WD masses and cooling ages are practically identical in the three cases, however the MS progenitor lifetimes significantly vary as function of metallicity. Note also that for ultra-massive WDs we used the sequence of [Camisassa et al. \(2019\)](#) for the three metallicities.

⁵ We fitted a fifth order polynomial between [Fe/H] and Z conversions, calculated assuming [Asplund et al. \(2005\)](#) solar abundances, resulting in $Z = 0.01230 + 0.02560 \times [\text{Fe}/\text{H}] + 0.03291 \times [\text{Fe}/\text{H}]^2 + 0.02833 \times [\text{Fe}/\text{H}]^3 + 0.01284 \times [\text{Fe}/\text{H}]^4 + 0.00223 \times [\text{Fe}/\text{H}]^5$.

cooling sequences of [Camisassa et al. \(2016\)](#). Taking into account the errors in effective temperature and surface gravity, we calculated the total age errors following the same approach.

It has to be emphasised that in this work we used a more updated set of cooling sequences as well as a different initial-to-final mass relation than in [Rebassa-Mansergas et al. \(2016b\)](#). Therefore, we have recalculated the total ages of the binaries studied in that work and included them in [Table 2](#). Moreover, as indicated in [Section 3.1.2](#), two SDSS WDMS binaries were only observed by the GTC using the EMIR spectrograph. In these two cases, in order to obtain the total ages, we used the WD effective temperatures and surface gravities reported by [Rebassa-Mansergas et al. \(2016a\)](#), which were derived by fitting the optical SDSS publicly available spectra of these two binaries.

Of the 52 SDSS WDMS binaries analysed here (23 from [Rebassa-Mansergas et al. 2016b](#)), 6 have masses $\lesssim 0.50 M_{\odot}$. Such low-mass WDs can not be formed via single stellar evolution because their progenitors have main sequence lifetimes longer than the Hubble time. Therefore, a binary origin involving mass transfer interactions is generally required to explain these objects (e.g. [Rebassa-Mansergas et al. 2011](#)). Because of this reason we can not derive the ages of these 6 systems. A possibility is that these unresolved SDSS WDMS binaries are in fact close binaries that evolved through a common envelope phase but have low inclinations, thus implying no radial velocity variation detection. This issue will be further discussed in [Section 5](#).

4.3 MS metallicities of the Gaia WDMS CPMP sample

We obtained 534 high-resolution spectra ([Table 1](#)) of 349 unique companion stars in our sample⁶, 26 of which have spectral types earlier than $\approx F0$, 260 are F, G or K-type stars, 6 are giants of luminosity class between III and IV, and 55 are M dwarfs (45 of spectral type M3 or earlier and 10 of spectral types M4–M5). The lack of near-infrared spectroscopy does not allow measuring the [Fe/H] abundances of the M dwarfs in the same way as we have performed for the SDSS sample. Hence, we attempted to measure the abundances of the 311 F, G, K and early M (M3 or earlier) as well as giant companions via detailed spectroscopic fits.

We determined the effective temperatures, surface gravities, microturbulent velocities and [Fe/H] abundances using the *rgvfit* code ([Takeda et al. 2005](#)). This routine implements the iron ionisation plus the iron equilibrium conditions as well as match of the curve of growth. Such a methodology is widely applied to solar-type stars of spectral types between F5 and K2/K3. We used a set of well-defined 302 Fe I and 28 Fe II lines in the analysis. The code makes use of ATLAS9, plane-parallel, local thermodynamic equilibrium (LTE) atmosphere models ([Kurucz 1993](#)). Uncertainties in the stellar parameters are statistical, that is, each stellar parameter is progressively changed from the converged solution until a value in which any of the aforementioned conditions is no longer fulfilled.

For low-mass stars, M dwarfs, we determined the stellar parameters using the procedures developed by [Maldonado et al. \(2015\)](#)⁷. In brief, this routine uses as a temperature diagnostic the ratios of pseudo-equivalent widths of spectral features, while calibrations for the stellar metallicity are derived from combinations and ratios of

⁶ Several targets were observed more than once at the same and/or different telescopes.

⁷ <https://github.com/jesumaldonadoprado/mdslines>

features. The temperatures and metallicities thus derived are used together with photometric estimates of surface gravity, mass and radius to calibrate empirical relations for these parameters.

The procedures described above converged to reliable fits in 235 of the cases. These companion stars are illustrated as black solid dots, as well as their WD primaries, in Figure 1. For the remaining 76 objects the available spectra were of too low signal-to-noise ratio ($\lesssim 30$), the number of measured Fe lines were too low, or there were problems in measuring and correcting the radial velocity for a proper determination of the [Fe/H] abundances. For those objects with more than one [Fe/H] determination from available multiple spectra, we used the average values. In the few cases where the individual [Fe/H] values considerably disagreed, we adopted the value corresponding to the spectrum with higher signal-to-noise ratio.

4.4 WD ages of the *Gaia* WDMS CPMP sample

Low-resolution optical spectra were obtained for 214 WDs at the WHT and INT telescopes (Table 1), however only 67 of their companions have available high-resolution MS spectra (Section 4.3). Of these 67 WDs, 15 are hydrogen-rich (DA) WDs that unfortunately have too noisy spectra for measurement of reliable stellar parameters, 14 are featureless (DC) WDs, 3 are helium-rich (DB) WDs, 1 is a metal-rich (DZ) WD and only 34 are hydrogen-rich (DA) WDs with good fits to their spectra. This implies we can only attempt to determine ages for 34 of the 235 binaries for which we have obtained a metallicity value (Section 4.3). As a consequence, rather than measuring the WD stellar parameters (hence ages) from their available good-quality spectra, we decided to derive them using the corresponding *Gaia* EDR3 (*Gaia* Collaboration et al. 2020; Riello et al. 2020) photometry and parallaxes⁸. Compared to using spectroscopy alone, this holds the potential of providing a factor ≈ 7 increase in the number of age-metallicity pairs.

All the WDs that are part of our *Gaia* WDMS CPMPs are associated to measured parallaxes and G , G_{BP} and G_{RP} magnitudes from *Gaia* EDR3. This allowed for derivations of the corresponding effective temperatures and surface gravities, hence masses and ages, by interpolating the observed G absolute magnitudes and $G_{BP} - G_{RP}$ colours in the cooling sequences developed by the La Plata group for pure-hydrogen atmospheres (see Section 4.2). The synthetic G , G_{BP} and G_{RP} absolute magnitudes were incorporated by us to the WD cooling sequences integrating the flux of the associated model atmosphere spectra (Koester 2010) over the corresponding EDR3 pass-bands. It has to be emphasised that before performing the interpolation the observed EDR3 magnitudes were corrected from extinction using the 3D maps of Lallement et al. (2014); Capitanio et al. (2017). As expected from their close distance, the extinction correction was rather low in most cases with an average value of $A_g = 0.04$ mag and a maximum correction of $A_g = 0.26$ mag, where A_g was obtained from A_V using the law of Fitzpatrick et al. (2019) and assuming $R_V = 3.1$. The effective temperature and surface gravity errors were obtained by propagating the parallax and photometric errors.

It is important to note that we find a relatively large fraction (≈ 19 per cent) of low-mass ($\lesssim 0.5 M_\odot$) WDs. This is intriguing since these are in resolved CPMP systems and their progenitors should have evolved like single stars, hence producing higher mass WDs. Half of the these presumably low-mass WDs have photometric effective

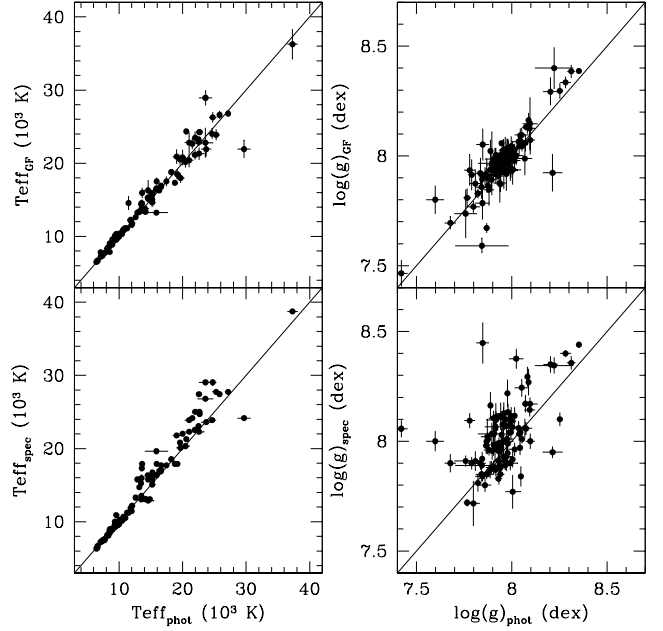


Figure 3. Top panels: a comparison between the WD effective temperatures (left) and surface gravities (right) measured in this work from *Gaia* EDR3 photometry and parallaxes as compared to those obtained by Gentile Fusillo et al. (2019) from *Gaia* DR2 data. Bottom panels: the same but comparing the photometric EDR3 values to those obtained from our follow-up spectroscopy.

temperatures under $\approx 6,000$ K, hence they could be non-DA WDs for which the age we measure is uncertain. A systematic shift towards low masses below $\approx 6,000$ K has also been reported by McCleery et al. (2020). For the hotter WDs, pure-helium DB models would yield even lower masses. Hence, a possible explanation is that the atmospheres of these WDs are not hydrogen- nor helium-dominated. Another possibility is that these objects are, or were, triple systems formed by an inner close binary (for example a double degenerate) and an outer MS companion. We will investigate these hypotheses in a separate publication.

An obvious question is whether the stellar parameters measured using both methods (spectroscopy and photometry) are consistent. To check this we derived the effective temperatures and surface gravities of 107 hydrogen-rich DA WDs that we observed at the WHT and INT in the same way as described in Section 4.2 (without the need of subtracting the MS companion contribution, since these are resolved WDs in CPMPs). Hereafter, we consider $T_{\text{eff-spec}}$ and $\log(g)_{\text{spec}}$ as the measured values from spectroscopy. The photometric parameters, $T_{\text{eff-phot}}$ and $\log(g)_{\text{phot}}$, were derived as described in the previous paragraphs from the available *Gaia* EDR3 data. In the bottom panels of Figure 3 we compare the stellar parameters thus obtained. If we define τ as

$$\tau = \frac{|\text{spec value} - \text{phot value}|}{\sqrt{\text{spec } \sigma^2 + \text{phot } \sigma^2}}, \quad (1)$$

where ‘value’ indicates either effective temperature or surface gravity and σ the corresponding errors, we find that the T_{eff} and $\log g$ measurements are consistent within 2τ for ≈ 30 and ≈ 50 per cent of the cases, respectively. Tremblay et al. (2020) argued that the photometric effective temperatures they measured for a sample of 89 *Gaia* DR2 hydrogen-rich WDs within 40 pc were 2.7 per cent underestimated as compared to their spectroscopic measurements. By considering this effect, the percentage of WDs with consistent spectroscopic and

⁸ Note that the *Gaia* WDMS CPMPs were selected using DR2 data (Figure 1). However, we used the newest EDR3 to measure the WD ages.

Table 3. Object names, WD and MS coordinates, WD effective temperatures, surface gravities and masses measured from *Gaia* photometry and spectroscopy (when available), the corresponding total ages and the MS star [Fe/H] abundances (assumed to be same as for the WD progenitors) of the 235 *Gaia* WDMS binaries analysed in this work. For 46 WDs the masses are too low to derive an age. The complete table can be found in the supplementary material, where the *Gaia* source IDs of each component are also provided.

Object	WD ra/dec (degrees)	MS ra/dec (degrees)	$T_{\text{eff-phot}}$ (K)	$\log g_{\text{phot}}$ (dex)	$\text{Mass}_{\text{phot}}$ (M_{\odot})	Age_{phot} (Gyr)	$T_{\text{eff-spec}}$ (K)	$\log g_{\text{spec}}$ (dex)	$\text{Mass}_{\text{spec}}$ (M_{\odot})	Age_{spec} (Gyr)	[Fe/H] (dex)
J0012+2328	2.96163/23.48678	3.00612/23.47178	8109±210	8.17±0.06	0.70 ^{+0.04} _{-0.04}	1.77 ^{+0.10} _{-0.08}	-	-	-	-	-0.18±0.03
J0021+2531	5.31779/25.52627	5.31696/25.52431	9332±126	8.49±0.03	0.90 ^{+0.02} _{-0.02}	1.57 ^{+0.02} _{-0.01}	-	-	-	-	0.16±0.05
J0033+4443	8.26320/44.73679	8.25721/44.72989	10198±164	7.98±0.03	0.59 ^{+0.02} _{-0.02}	1.99 ^{+0.48} _{-1.83}	10141±63	8.07±0.06	0.64 ^{+0.03} _{-0.04}	1.35 ^{+0.12} _{-0.29}	-0.03±0.02
J0045+1421	11.34235/14.34570	11.33858/14.36269	4886±34	7.81±0.02	0.49 ^{+0.01} _{-0.01}	-	-	-	-	-	-0.26±0.03
J0048+1333	12.18230/13.55794	12.18096/13.55589	12588±1543	8.45±0.14	0.88 ^{+0.09} _{-0.38}	0.65 ^{+0.06} _{-0.06}	-	-	-	-	0.27±0.5
J0055+3321	13.81336/33.35159	13.81654/33.35214	18190±1274	7.90±0.08	0.55 ^{+0.04} _{-0.04}	6.50 ^{+2.60} _{-5.80}	-	-	-	-	0.42±0.04
J0103+6108	15.79464/61.12871	15.79292/61.13567	9317±270	8.02±0.06	0.61 ^{+0.03} _{-0.03}	1.48 ^{+0.14} _{-1.36}	-	-	-	-	-0.10±0.03
J0108+7018	17.12171/70.30084	17.13725/70.30042	5351±154	7.93±0.09	0.55 ^{+0.03} _{-0.04}	10.21 ^{+1.79} _{-2.83}	-	-	-	-	-0.11±0.04
J0112+0454	18.03588/4.91914	18.03363/4.91625	19160±744	8.07±0.04	0.66 ^{+0.02} _{-0.02}	0.68 ^{+0.13} _{-0.15}	20098±211	8.06±0.04	0.65 ^{+0.02} _{-0.02}	0.69 ^{+0.13} _{-0.13}	-0.03±0.04
J0115+1534	18.98383/15.58056	18.98204/15.58008	24039±577	7.95±0.02	0.59 ^{+0.01} _{-0.01}	5.65 ^{+1.20} _{-1.03}	-	-	-	-	0.63±0.13
J0119+6218	19.83586/62.30148	19.83471/62.30539	16166±336	7.94±0.03	0.57 ^{+0.02} _{-0.01}	7.55 ^{+2.21} _{-0.14}	-	-	-	-	0.41±0.03

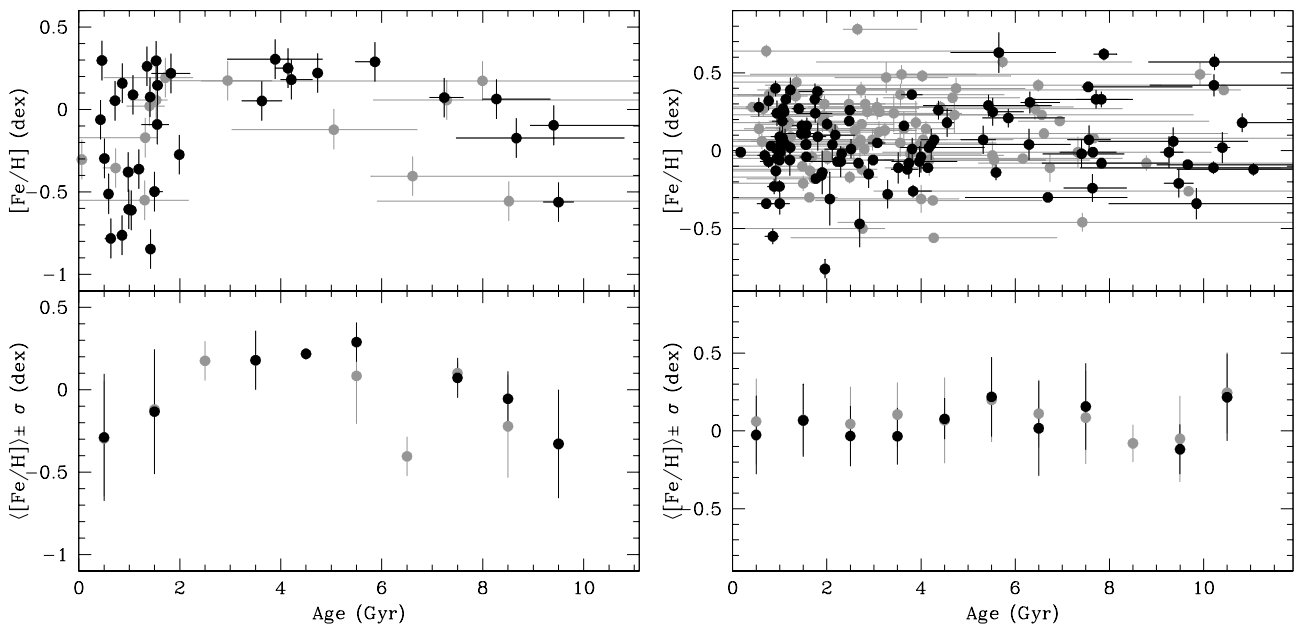


Figure 4. Top left panel: the age-metallicity relation obtained from SDSS WDMS binaries. Black dots represent ages with relative errors less than 30 per cent. Bottom left panel: average [Fe/H] values for 1 Gyr bins, together with their standard deviations for the entire sample (grey) and for the sample with age relative errors below 30 per cent (black). Right panels: the same but for *Gaia* WDMS CPMs.

photometric effective temperatures in our sample increases from ≈ 30 to ≈ 45 per cent. The percentages of agreement within 2τ further increase to ≈ 70 per cent for both T_{eff} and $\log g$ if we systematically add a 0.015 dex uncertainty to the $\log g$ measurements and a 150 K uncertainty to the effective temperature values. This clearly reveals the effect the small errors in our measurements have in quantifying the degree of consistency between the two methods. We thus conclude that the spectroscopic and photometric measurements are broadly consistent. We will further discuss this issue in Section 5.

For completeness, we show in the top panels of Fig. 3 the comparison between our photometric values and those obtained from *Gaia* DR2 data by Gentile Fusillo et al. (2019). Visual inspection suggests the two sets of data are in good agreement. Indeed, in $\approx 75/85$ per cent of the cases the effective temperature/surface gravity measurements are consistent within 2τ .

5 DISCUSSION: THE AGE-METALLICITY RELATION

The AMR that results from the SDSS WDMS binary sample is shown in the top left panel of Figure 4, where a clear scatter of [Fe/H] abundances (>0.2 dex) is observed at most ages. This is corroborated in the bottom left panel of the same figure, where we show the average [Fe/H] per 1 Gyr bin. It is worth noting that in ≈ 20 per cent of the cases the age measurements are subjected to substantial uncertainties (>30 per cent of relative error; grey points in Figure 4). This is due to the relatively large uncertainties in the measured WD parameters that translate into larger age uncertainties and, mainly, due to the fact that the determined WD masses are low ($\lesssim 0.55 M_{\odot}$). The lower the WD mass, the longer its progenitor spent on the MS. This MS lifetime is very sensitive to the mass of the WD progenitor star, thus even small errors in the derived WD masses translate into rather different ages spent on the MS and, as a consequence, into larger total

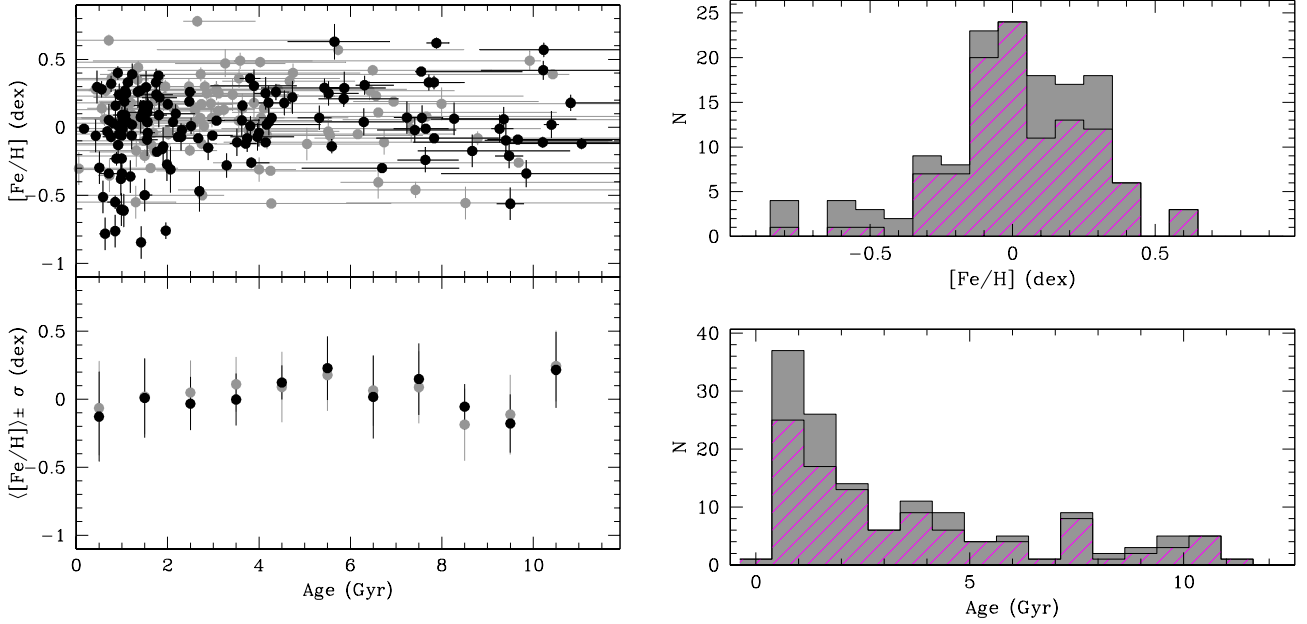


Figure 5. Left panels: the same as Figure 4 but for the entire sample studied in this work (46 SDSS WDMS binaries plus 189 *Gaia* WDMS CPMPs). There is no correlation between age and metallicity. Right panels: the age (bottom; relative error less than 30 per cent) and $[\text{Fe}/\text{H}]$ abundance (top) corresponding distributions. For comparative purposes the age and $[\text{Fe}/\text{H}]$ abundance distributions for the *Gaia* WDMS binary sample are shown in magenta.

age uncertainties. Given that low-mass WDs evolve from low-mass MS stars that require a longer time to leave the main sequence, the percentage of ages with larger uncertainties is higher for intermediate and old ages ($\gtrsim 5$ Gyr).

It is also important to mention that these unresolved SDSS WDMS binaries are expected to have evolved avoiding mass transfer episodes based on the lack of radial velocity variations. However, as discussed in Section 4.2, it is possible that a small number of the SDSS WDMS systems are in fact post common envelope binaries with low orbital inclinations (preventing the detection of radial velocity variations). For those systems, the measured ages would not be accurate. The probability of non-detection of a close WDMS binary due to a low-inclination is ≈ 15 per cent (Nebot Gómez-Morán et al. 2011). This could explain why the three most metal-poor stars in the sample ($[\text{Fe}/\text{H}] < -0.7$ dex) appear to be younger than 2 Gyrs.

The *Gaia* WDMS CPMP AMR is illustrated in the top right panel of Figure 4 and the corresponding average $[\text{Fe}/\text{H}]$ per 1 Gyr bin in the bottom right panel. In the same way as we have observed for the SDSS sample, the scatter of $[\text{Fe}/\text{H}]$ abundances becomes apparent at all ages. It has to be noted that the WD ages for this sample were obtained from the available *Gaia* EDR3 photometry and that the WD stellar parameters obtained from these data are found to be broadly consistent with those obtained from the spectroscopic fits (Section 4.4). To investigate whether or not this issue affects the result obtained, we derived the (spectroscopic) WD ages of the 34 DA WDs for which the stellar parameters are also measured from spectroscopy (Section 4.4). These values are included in Table 3. We found the same scatter of $[\text{Fe}/\text{H}]$ despite the fact that the individual ages vary, as expected, for some objects. Therefore, we can safely conclude that the scatter of metallicities in the *Gaia* WDMS CPMP AMR is real.

It is also important to emphasise that the WD cooling sequences we have adopted to determine the stellar parameters are those developed for hydrogen-rich DA WDs. The lack of spectroscopy does not

allow us to confirm this assumption for those WDs with only *Gaia* photometry available. Thus, we expect a fraction of non-DA WDs in our sample. From our spectroscopic sub-sample of 67 objects, we calculate fractions of ≈ 73 per cent DAs, ≈ 4 per cent DBs, ≈ 1 per cent DZs and ≈ 20 per cent DCs, although the latter (visual) classification is likely biased because of signal-to-noise ratio issues of the spectra. Assuming these fractions are the same for the entire *Gaia* WDMS CPMP sample, we reach the following conclusions: (i) ≈ 4 per cent of our ages are underestimated because we are using pure-hydrogen sequences to derive the ages of DB WDs. This is because photometric masses obtained assuming pure-helium DB sequences are generally lower than those obtained using pure-hydrogen models (Gentile Fusillo et al. 2019). This implies lower MS progenitor masses and larger progenitor lifetimes as compared to those obtained using pure-hydrogen models; (ii) given that ≈ 40 per cent of WDs have He-rich atmospheres at $\approx 5,000 - 7000$ K (McCleery et al. 2020), we expect approximately half of the spectroscopically (visually) classified objects as DC WDs to have He-dominated atmospheres. This implies an additional ≈ 10 per cent of underestimated ages in the total sample; (iii) ≈ 1 per cent of the WDs are expected to have other atmospheric composition apart from hydrogen and helium, such as DZ WDs. In these cases the derived ages are uncertain. In summary, we expect ≈ 14 per cent of the *Gaia* WDMS CPMP ages to be underestimated and ≈ 1 per cent to be uncertain.

In the top left panel of Fig. 5 we show the AMR that results from combining our SDSS and the full *Gaia* WDMS binary samples, a total of 235 age- $[\text{Fe}/\text{H}]$ pairs. The average $[\text{Fe}/\text{H}]$ abundances per Gyr bin and the standard deviations are shown in the left bottom panel of the same figure and provided in Table 4. The sample is dominated by young objects ($\lesssim 5$ Gyr; see bottom right panel of Fig. 5), but it also samples both intermediate and old ages. Unfortunately, very few objects in our total sample have ages larger than 10 Gyr, which does not allow us to study the properties of the AMR relation for very old ages in a robust way. The drop of systems with ages > 10 Gyr can

be understood as follows. In order to achieve an age longer than 10 Gyrs a WD requires one of the following properties: (1) a very low mass ($\approx 0.5 M_{\odot}$) thus implying a very long main sequence progenitor lifetime and a short cooling age (hence a relatively hot temperature; $>10,000$ K); (2) a very cool effective temperature (≤ 4000 K), thus implying a long cooling age and a short progenitor lifetime (hence a relatively more massive white dwarf; $\gtrsim 0.6 M_{\odot}$); (3) a low mass ($\approx 0.55 M_{\odot}$) and a low effective temperature (~ 6000 K). As explained in Section 2, the SDSS WDMS sample suffers from selection effects against cool WDs and therefore the probability for detecting very old age systems decreases. For the *Gaia* population, we are analysing objects with average distances of 150 pc (Section 2), which defines a sample close to be volume-limited. In a volume-limited sample not only hot WDs ($>10,000$ K) are intrinsically less numerous but also the completeness of cold (<5000 K) and less luminous WDs decreases to ≈ 60 per cent (Torres et al. 2021). These effects imply that, overall, it becomes intrinsically more difficult to find WDs with ages longer than 10 Gyrs.

Like Casagrande et al. (2011), we find no steep decline in metallicity for ages in the ≈ 9 -10 Gyr range, a trend that was reported by Bergemann et al. (2014). The AMR we obtained fluctuates between approximately -0.5 and $+0.5$ dex with a peak centered at around $[\text{Fe}/\text{H}]=0$ (see the top right panel of Fig. 5) and, as expected from the previous discussion, it does not show any apparent correlation. This result is in agreement with several previous studies that analysed the AMR in which the ages were derived from Strömberg photometry (Feltzing et al. 2001; Nordström et al. 2004; Casagrande et al. 2011), spectroscopy and luminosities obtained via parallaxes (Buder et al. 2019; Delgado Mena et al. 2019; Nissen et al. 2020), isochrone matching (Hayden et al. 2020), open clusters (Carraro et al. 1998; Pancino et al. 2010) and asteroseismology (Silva Aguirre et al. 2018; Miglio et al. 2021). The analysis performed in this work using a different technique for measuring stellar ages reaches the same conclusion. Self-enrichment of gas in star forming regions (Pilyugin & Edmunds 1996) or episodic gas in-fall onto the disc (Köppen & Hensler 2005) are proposed physical mechanisms to explain the lack of correlation between age and metallicity in the solar neighbourhood. However, the most accepted scenario invokes radial migration, a physical mechanism in which metal-rich stars that form in the inner disc migrate to the outer and metal-poorer disc (Sellwood & Binney 2002; Roškar et al. 2008; Minchev et al. 2011, 2013; Feuillet et al. 2019). The validity of this scenario is further supported by the fact that our AMR displays young (≈ 1 Gyr) but metal-rich ($[\text{Fe}/\text{H}]>2$ dex) objects (left panel of Fig. 5). It is widely accepted that such stars cannot form in the solar neighbourhood and, as a consequence, must have migrated from a more metal-rich environment in the inner Galaxy (Haywood 2008; Brunetti et al. 2011).

6 CONCLUSIONS

Dating a star is a challenging task. For decades, this difficult endeavour has been pursued for single stars using different techniques, which has allowed analysing the observational properties of the age-metallicity relation in the solar neighbourhood. These studies seem to converge to the same result, i.e. there is no correlation between age and metallicity as traced by the $[\text{Fe}/\text{H}]$ abundances. In this work we have used an alternative way for measuring stellar ages based on the analysis of white dwarf-main sequence binaries from which we can obtain accurate white dwarf ages and main sequence $[\text{Fe}/\text{H}]$ abundances. The age-metallicity relation that we have obtained displays a scatter of approximately ± 0.5 dex at all ages. This is yet

Table 4. $\langle[\text{Fe}/\text{H}]\rangle \pm \sigma$ for 1 Gyr bins obtained from the full WDMS binary sample studied in this work. Only the age values with relative uncertainties under 30 per cent have been considered (black solid dots in the bottom panel of Fig. 5). For completeness, we also provide the values for the *Gaia* and SDSS samples.

	Full sample	<i>Gaia</i> sample	SDSS sample
Age (Gyr)	$\langle[\text{Fe}/\text{H}]\rangle \pm \sigma$ (dex)	$\langle[\text{Fe}/\text{H}]\rangle \pm \sigma$ (dex)	$\langle[\text{Fe}/\text{H}]\rangle \pm \sigma$ (dex)
0.5	-0.13 ± 0.33	-0.03 ± 0.25	-0.29 ± 0.39
1.5	0.01 ± 0.29	0.07 ± 0.23	-0.13 ± 0.38
2.5	-0.03 ± 0.19	-0.03 ± 0.19	-
3.5	0.00 ± 0.19	-0.03 ± 0.18	0.18 ± 0.18
4.5	0.12 ± 0.13	0.08 ± 0.13	0.22 ± 0.03
5.5	0.23 ± 0.23	0.22 ± 0.26	0.29 ± 0.12
6.5	0.02 ± 0.31	0.02 ± 0.31	-
7.5	0.15 ± 0.26	0.16 ± 0.28	0.07 ± 0.12
8.5	-0.06 ± 0.17	-	-0.06 ± 0.17
9.5	-0.18 ± 0.21	-0.12 ± 0.16	-0.33 ± 0.33
10.5	0.22 ± 0.28	0.22 ± 0.28	-

another robust confirmation of the lack of correlation between age and metallicity in the solar neighbourhood.

ACKNOWLEDGMENTS

Project supported by a 2019 Leonardo Grant for Researchers and Cultural Creators, BBVA Foundation. The Foundation accepts no responsibility for the opinions, statements and contents included in the project and/or the results thereof, which are entirely the responsibility of the authors.

ARM acknowledges additional support from the MINECO under the Ramón y Cajal program (RYC-2016-20254). JM acknowledges support from the Accordo Attuativo ASI-INAF n. 2018.22.HH.O, Partecipazione alla fase B1 della missione Ariel. RR has received funding from the postdoctoral fellowship programme Beatriu de Pinós, funded by the Secretary of Universities and Research (Government of Catalonia) and by the Horizon 2020 programme of research and innovation of the European Union under the Maria Skłodowska-Curie grant agreement No 801370. ST acknowledges support from the MINECO under the AYA2017-86274-P grant, and the AGAUR grant SGR-661/2017. MJH was supported by the UK Science and Technology Facilities Council studentship ST/R505195/1. BTG was supported by a Leverhulme Research Fellowship and the UK STFC grant ST/T000406/1. PET, TC and MH have received funding from the European Research Council under the European Union’s Horizon 2020 research and innovation programme n. 677706 (WD3D).

Based on observations made with the Gran Telescopio Canarias (GTC; programmes GTC6-16B, GTC1-17A, GTC26-17B and GTC6-18A), installed in the Spanish Observatorio del Roque de los Muchachos of the Instituto de Astrofísica de Canarias, in the island of La Palma. This work is based on observations made with ESO Telescopes at the La Silla Paranal Observatory under programme ID 0101.B-0130. Based on observations made with the Telescopio Nazionale Galileo and Mercator Telescope awarded to the International Time Programme ITP18_8. Based on observations made with the William Herschel Telescope (programmes C12 and C26) and Isaac Newton Telescope (programme P4W) operated on the island of La Palma by the Isaac Newton Group of Telescopes in the Spanish Observatorio del Roque de los Muchachos of the Instituto de

Astrofísica de Canarias. We acknowledge the support of the staff of the Xinglong 2.16 m telescope. This work was partially supported by the Open Project Program of the Key Laboratory of Optical Astronomy, National Astronomical Observatories, Chinese Academy of Sciences.

MJH acknowledges Saskia Prins, the support astronomer at Mercator for her invaluable help.

This work has made use of data from the European Space Agency (ESA) mission *Gaia* (<https://www.cosmos.esa.int/gaia>), processed by the *Gaia* Data Processing and Analysis Consortium (DPAC, <https://www.cosmos.esa.int/web/gaia/dpac/consortium>). Funding for the DPAC has been provided by national institutions, in particular the institutions participating in the *Gaia* Multilateral Agreement.

DATA AVAILABILITY

The data underlying this article are available in the manuscript. Supplementary material will be shared on reasonable request to the corresponding author.

REFERENCES

- Althaus L. G., Córscico A. H., Isern J., García-Berro E., 2010, *A&ARv*, **18**, 471
- Althaus L. G., Camisassa M. E., Miller Bertolami M. M., Córscico A. H., García-Berro E., 2015, *A&A*, **576**, A9
- Andrews J. J., Chanamé J., Agüeros M. A., 2017, *MNRAS*, **472**, 675
- Asplund M., Grevesse N., Sauval A. J., 2005, in Barnes III T. G., Bash F. N., eds, *Astronomical Society of the Pacific Conference Series Vol. 336, Cosmic Abundances as Records of Stellar Evolution and Nucleosynthesis*, p. 25
- Barrientos M., Chanamé J., 2021, arXiv e-prints, p. arXiv:2102.07790
- Barry D. C., 1988, *ApJ*, **334**, 436
- Bensby T., Feltzing S., Oey M. S., 2014, *A&A*, **562**, A71
- Bergemann M., et al., 2014, *A&A*, **565**, A89
- Brunetti M., Chiappini C., Pfenninger D., 2011, *A&A*, **534**, A75
- Buder S., et al., 2019, *A&A*, **624**, A19
- Camisassa M. E., Althaus L. G., Córscico A. H., Vinyoles N., Serenelli A. M., Isern J., Miller Bertolami M. M., García-Berro E., 2016, *ApJ*, **823**, 158
- Camisassa M. E., et al., 2019, *A&A*, **625**, A87
- Capitanio L., Lallement R., Vergely J. L., Elyajouri M., Monreal-Ibero A., 2017, *A&A*, **606**, A65
- Carraro G., Ng Y. K., Portinari L., 1998, *MNRAS*, **296**, 1045
- Casagrande L., Schönrich R., Asplund M., Cassisi S., Ramírez I., Meléndez J., Bensby T., Feltzing S., 2011, *A&A*, **530**, A138
- Casagrande L., et al., 2016, *MNRAS*, **455**, 987
- Catalán S., Isern J., García-Berro E., Ribas I., 2008, *MNRAS*, **387**, 1693
- Cosentino R., et al., 2012, in McLean I. S., Ramsay S. K., Takami H., eds, *Society of Photo-Optical Instrumentation Engineers (SPIE) Conference Series Vol. 8446, Ground-based and Airborne Instrumentation for Astronomy IV*, p. 84461V, doi:10.1117/12.925738
- Cummings J. D., Kalirai J. S., Tremblay P. E., Ramirez-Ruiz E., Choi J., 2018, *ApJ*, **866**, 21
- Delgado Mena E., et al., 2019, *A&A*, **624**, A78
- Edvardsson B., Andersen J., Gustafsson B., Lambert D. L., Nissen P. E., Tomkin J., 1993, *A&A*, **275**, 101
- Eisenstein D. J., et al., 2011, *AJ*, **142**, 72
- El-Badry K., Rix H.-W., 2018, *MNRAS*, **480**, 4884
- El-Badry K., Rix H.-W., Heintz T. M., 2021, *MNRAS*,
- Fan Z., et al., 2016, *PASP*, **128**, 115005
- Feltzing S., Chiba M., 2013, *New Astron. Rev.*, **57**, 80
- Feltzing S., Holmberg J., Hurley J. R., 2001, *A&A*, **377**, 911
- Feuillet D. K., Frankel N., Lind K., Frinchaboy P. M., García-Hernández D. A., Lane R. R., Nitschelm C., Roman-Lopes A., 2019, *MNRAS*, **489**, 1742
- Fitzpatrick E. L., Massa D., Gordon K. D., Bohlin R., Clayton G. C., 2019, *ApJ*, **886**, 108
- Fouesneau M., Rix H.-W., von Hippel T., Hogg D. W., Tian H., 2019, *ApJ*, **870**, 9
- Gaia Collaboration et al., 2016, *A&A*, **595**, A1
- Gaia Collaboration et al., 2018a, *A&A*, **616**, A1
- Gaia Collaboration et al., 2018b, *A&A*, **616**, A10
- Gaia Collaboration Brown A. G. A., Vallenari A., Prusti T., de Bruijne J. H. J., Babusiaux C., Biermann M., 2020, arXiv e-prints, p. arXiv:2012.01533
- Gentile Fusillo N. P., et al., 2019, *MNRAS*, **482**, 4570
- Hayden M. R., et al., 2020, arXiv e-prints, p. arXiv:2011.13745
- Haywood M., 2008, *MNRAS*, **388**, 1175
- Haywood M., Di Matteo P., Lehnert M. D., Katz D., Gómez A., 2013, *A&A*, **560**, A109
- Holtzman J. A., et al., 2015, *AJ*, **150**, 148
- Howes L. M., Lindegren L., Feltzing S., Church R. P., Bensby T., 2019, *A&A*, **622**, A27
- Jiménez-Esteban F. M., Solano E., Rodrigo C., 2019, *AJ*, **157**, 78
- Jørgensen B. R., Lindegren L., 2005, *A&A*, **436**, 127
- Koester D., 2010, *Mem. Soc. Astron. Italiana*, **81**, 921
- Köppen J., Hensler G., 2005, *A&A*, **434**, 531
- Kurucz R., 1993, *ATLAS9 Stellar Atmosphere Programs and 2 km/s grid*. Kurucz CD-ROM No. 13. Cambridge, 13
- Lallement R., Vergely J. L., Valette B., Puspitarini L., Eyer L., Casagrande L., 2014, *A&A*, **561**, A91
- Lam M. C., Hambly N. C., Lodieu N., Blouin S., Harvey E. J., Smith R. J., Gálvez-Ortiz M. C., Zhang Z. H., 2020, *MNRAS*, **493**, 6001
- Lindegren L., 2018, Technical Report GAIA-C3-TN-LU-LL-124-01, Re-normalising the astrometric chi-square in *Gaia* DR2, http://www.rssd.esa.int/doc_fetch.php?id=3757412. Lund Observatory, Lund, Sweden, http://www.rssd.esa.int/doc_fetch.php?id=3757412
- Lindgren S., Heiter U., 2017, *A&A*, **604**, A97
- Maldonado J., et al., 2015, *A&A*, **577**, A132
- Marsh T. R., 1989, *PASP*, **101**, 1032
- McCleery J., et al., 2020, *MNRAS*, **499**, 1890
- Miglio A., et al., 2021, *A&A*, **645**, A85
- Miller Bertolami M. M., 2016, *A&A*, **588**, A25
- Minchev I., Famaey B., Combes F., Di Matteo P., Mouhcine M., Wozniak H., 2011, *A&A*, **527**, A147
- Minchev I., Chiappini C., Martig M., 2013, *A&A*, **558**, A9
- Nebot Gómez-Morán A., et al., 2011, *A&A*, **536**, A43
- Newton E. R., Charbonneau D., Irwin J., Berta-Thompson Z. K., Rojas-Ayala B., Covey K., Lloyd J. P., 2014, *AJ*, **147**, 20
- Nissen P. E., Christensen-Dalsgaard J., Mosumgaard J. R., Silva Aguirre V., Spitoni E., Verma K., 2020, *A&A*, **640**, A81
- Nomoto K., Kobayashi C., Tominaga N., 2013, *ARA&A*, **51**, 457
- Nordström B., et al., 2004, *A&A*, **418**, 989
- Pancino E., Carrera R., Rossetti E., Gallart C., 2010, *A&A*, **511**, A56
- Parsons S. G., et al., 2012, *MNRAS*, **426**, 1950
- Pickles A. J., 1998, *PASP*, **110**, 863
- Pilyugin L. S., Edmunds M. G., 1996, *A&A*, **313**, 792
- Pinsonneault M. H., et al., 2018, *ApJS*, **239**, 32
- Qiu D., Tian H.-J., Wang X.-D., Nie J.-L., von Hippel T., Liu G.-C., Fouesneau M., Rix H.-W., 2020, arXiv e-prints, p. arXiv:2012.04890
- Raskin G., et al., 2011, *A&A*, **526**, A69
- Rebassa-Mansergas A., Gänsicke B. T., Rodríguez-Gil P., Schreiber M. R., Koester D., 2007, *MNRAS*, **382**, 1377
- Rebassa-Mansergas A., Gänsicke B. T., Schreiber M. R., Koester D., Rodríguez-Gil P., 2010, *MNRAS*, **402**, 620
- Rebassa-Mansergas A., Nebot Gómez-Morán A., Schreiber M. R., Girven J., Gänsicke B. T., 2011, *MNRAS*, **413**, 1121
- Rebassa-Mansergas A., Ren J. J., Parsons S. G., Gänsicke B. T., Schreiber M. R., García-Berro E., Liu X. W., Koester D., 2016a, *MNRAS*, **458**, 3808

- Rebassa-Mansergas A., et al., 2016b, *MNRAS*, **463**, 1137
- Renedo I., Althaus L. G., Miller Bertolami M. M., Romero A. D., Córscico A. H., Rohrmann R. D., García-Berro E., 2010, *ApJ*, **717**, 183
- Riello M., et al., 2020, arXiv e-prints, p. [arXiv:2012.01916](https://arxiv.org/abs/2012.01916)
- Rocha-Pinto H. J., Maciel W. J., Scalo J., Flynn C., 2000, *A&A*, **358**, 850
- Roškar R., Debattista V. P., Quinn T. R., Stinson G. S., Wadsley J., 2008, *ApJ*, **684**, L79
- Sellwood J. A., Binney J. J., 2002, *MNRAS*, **336**, 785
- Silva Aguirre V., et al., 2018, *MNRAS*, **475**, 5487
- Soubiran C., Bienaymé O., Mishenina T. V., Kovtyukh V. V., 2008, *A&A*, **480**, 91
- Takeda Y., Ohkubo M., Sato B., Kambe E., Sadakane K., 2005, *PASJ*, **57**, 27
- Teixeira G. D. C., Sousa S. G., Tsantaki M., Monteiro M. J. P. F. G., Santos N. C., Israelian G., 2016, *A&A*, **595**, A15
- Tody D., 1986, in Crawford D. L., ed., Society of Photo-Optical Instrumentation Engineers (SPIE) Conference Series Vol. 627, Instrumentation in astronomy VI. p. 733, [doi:10.1117/12.968154](https://doi.org/10.1117/12.968154)
- Torres S., Rebassa-Mansergas A., Camisassa M. E., Raddi R., 2021, *MNRAS*, **502**, 1753
- Tremblay P. E., Ludwig H. G., Steffen M., Freytag B., 2013, *A&A*, **559**, A104
- Tremblay P. E., et al., 2020, *MNRAS*, **497**, 130
- Twarog B. A., 1980, *ApJ*, **242**, 242
- Vernet J., et al., 2011, *A&A*, **536**, A105
- Willems B., Kolb U., 2004, *A&A*, **419**, 1057
- Wojno J., et al., 2018, *MNRAS*, **477**, 5612
- Wu Y., Xiang M., Chen Y., Zhao G., Bi S., Li C., Li Y., Huang Y., 2021, *MNRAS*, **501**, 4917
- York D. G., et al., 2000, *AJ*, **120**, 1579
- Yuan H., Liu X., Xiang M., Huang Y., Chen B., Wu Y., Hou Y., Zhang Y., 2015, *ApJ*, **799**, 135

This paper has been typeset from a $\text{\TeX}/\text{\LaTeX}$ file prepared by the author.